Nucleophilic Substitution Enables MXene Maximum Capacitance and Improved Stability

Jiang Xu,* Ryan S. Longchamps, Xi Wang, Bingqing Hu, Xude Li, Shijian Wang, Lvzhou Li, Yaokai Gu, Xiaoting Cao, Ningyi Yuan, Shanhai Ge,* Guoxiu Wang,* and Jianning Ding*

Combining the merits of battery and supercapacitor into a single device represents a major scientific and technological challenge. From a design perspective, electrode material plays a key role in the device and the fundamental difficulty lies in incorporating a high density of active sites into a stable material with excellent charge transfer kinetics. Here, the synthesis is reported of a nearly full-oxygen-functionalized 2D conductive transition metal carbide ($Ti_3C_2O_y$) with ultrahigh density of Ti—O/=O redox-active sites by nucleophilic substitution and in situ oxidation under the presence of a proper electrophilic reagent (K^+). The fabricated electrode delivered exceptionally high gravimetric and volumetric capacitance (1,082 F g^{-1} and 3,182 F cm^{-3} in a potential window of 0.85 V, approximating the theoretical capacity of many transition metal oxides), fast charging/discharging in tens of seconds across a wide range of temperature (−70 to 60 °C), and excellent structural and chemical stability. These promising results provide avenues for the development of high-energy, high-power storage devices as well as electromagnetic shielding, and electronic and optoelectronic devices.

1. Introduction

Increasing demand for portable and clean energy continually drives energy storage materials advancement.[1] Designing materials for electrochemical energy storage with short charging times and high charge capacities is a longstanding challenge.[2]

Electrochemical capacitors, known as supercapacitors, represent an important class of energy storage systems due to their extreme power density and extended cycle life, compared to Li-ion batteries.[3–5] However, traditional electrical double-layer capacitors (EDLCs), in which the capacitance stems from the electro-sorption of ions at the electrode/electrolyte interface, often suffer from limited specific capacitance and low energy density. An alternative sub-class of supercapacitors, pseudo-capacitors, offers a route to higher specific capacitance and energy density, owing to the storage of charge via fast and reversible surface redox reactions.[6,7] For example, transition metal oxides (RuO_2,[8,9] MnO_2,[9,10] Nb_2O_5,[11] etc.[6,12–14]), which could theoretically provide a specific capacity of more than 1000 C g^{-1} via metal redox reactions when used as pseudo-capacitive electrode materials.[6,15] However, low electrical conductivity and bulk material have stifled power performance[16] and limited the utilization of their theoretical storage capacity thus far (**Figure 1a**). Carbon nanomaterials[17] and nanoporous metal[8,10] have been introduced to increase conductivity, while particle size reduction[18] or fabrication of metal-organic frameworks (MOFs)[19] have been adopted to expose more redox active

J. Xu, X. Wang, L. Li, X. Cao, J. Ding
Institute of Technology for Carbon Neutralization
College of Electrical, Energy and Power Engineering
Yangzhou University
Yangzhou 225127, P. R. China
E-mail: xuj@yzu.edu.cn; dingjn@yzu.edu.cn

R. S. Longchamps, S. Ge
Department of Mechanical Engineering
The Pennsylvania State University
University Park, PA 16802, USA
E-mail: sug13@psu.edu

B. Hu, X. Li, Y. Gu, J. Ding
School of Mechanical Engineering
Jiangsu University
Zhenjiang 212013, P. R. China

S. Wang, G. Wang
Centre for Clean Energy Technology
School of Mathematical and Physical Sciences
Faculty of Science
University of Technology Sydney
Sydney, NSW 2007, Australia
E-mail: guoxiu.wang@uts.edu.au

N. Yuan, J. Ding
Jiangsu Collaborative Innovation Center of Photovoltaic Science and Engineering
Changzhou University
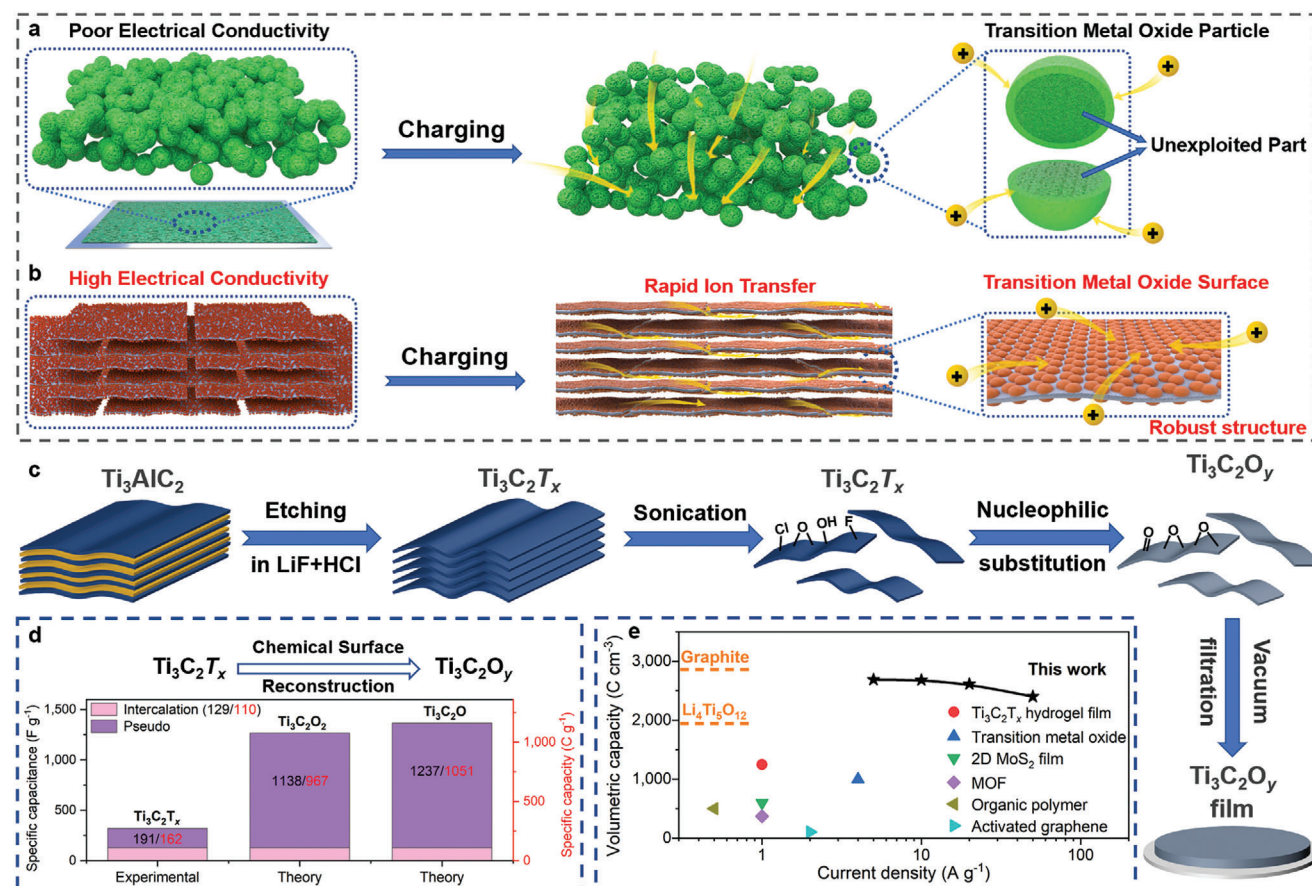Changzhou 213164, P. R. China

Figure 1. Schematic of pseudo-capacitive energy storage in 2D materials with transition metal oxides-like surface. A,b) Schematic of the traditional transition metal oxides electrode (a) and the electrode fabricated from the 2D materials with atomic level transition metal oxides surface, high electrical conductivity, and robust substrate (b). c) Synthesis scheme of $Ti_3C_2O_y$. d) The specific capacitance/capacity of the pristine $Ti_3C_2T_x$ and the theoretical specific capacitances/capacities of $Ti_3C_2O_y$ assuming a potential window of 0.85 V (Note S1, Supporting information for calculation). e) Volumetric capacity of several typical supercapacitance materials, including $Ti_3C_2T_x$ hydrogel film,[22] transition metal oxides,[10] 2D MoS2 quantum-sheet film,[41] metal–organic framework (MOF),[19] organic polymer[41] and activated graphene,[42] graphite and $Li_4Ti_5O_{12}$. For graphite and $Li_4Ti_5O_{12}$, the volumetric capacities are calculated based on both theory capacity and density.

sites. Unfortunately, these strategies render moderate improvements. It remains a great challenge to simultaneously achieve high specific and volumetric capacitance, high-rate capability, and long cycle stability.

2D materials are of particular interest in the pursuit of high-power, high-capacity alternatives, owing to their large electrochemically active surfaces.[20] MXenes[21] – a well-known class of 2D inorganic compounds with robust transition metal carbide/nitride substrate and abundant superficial functional groups – have high electrical conductivity up to 25000 S cm^{-1} and redox-active sites evenly distributed on the surface, offering a promising option for high-rate performance. However, this 2D material has been limited to a moderate specific capacitance of ≈380 F g^{-1} (323 C g^{-1}) for a potential window of 0.85 V,[22] owing to the non-optimal terminal groups.[22–24] Several methods have been investigated and proved to enhance the energy storage of the pristine MXenes, for example, partial oxidation,[25] atomic surface reduction,[26] expanding interlayer spacing,[27] etc.[23,24,28,29]

In this work, we designed and prepared a novel MXene with nearly 100% —O superficial functional groups to achieve a

transition metal oxide-like surface and near-theoretical specific capacitance while simultaneously offering high electrical conductivity (Figure 1b). We chose Ti_3C_2, a representative member of the MXene family,[21–24] as a model material to demonstrate this structure design since the theoretical specific capacitances of $Ti_3C_2O_2$ (1267 F g^{-1}; 1077 C g^{-1}) and Ti_3C_2O (1366 F g^{-1}; 1161 C g^{-1}) are exceed kilofarad per gram assuming a potential window of 0.85 V (Note S1, Supporting information), as opposed to the previously reported 380 F g^{-1} (323 C g^{-1}) for the precursor material, $Ti_3C_2T_x$ (T=OH, F, Cl, and O; Figure 1c,d).[22] Moreover, the volumetric capacity of $Ti_3C_2O_y$ (1≤y≤2) dwarfs that of alternative materials, offering a 2x-35x increase (Figure 1e).

2. Results and Discussion

2.1. Synthesis of the Nearly Full-Oxygen-Functionalized MXene

$Ti_3C_2T_x$ was first prepared as a precursor material for comparison and production of a "pristine" $Ti_3C_2T_x$ film and the $Ti_3C_2O_y$ (1≤y≤2) film, herein (Figure 1c). The chemical surface

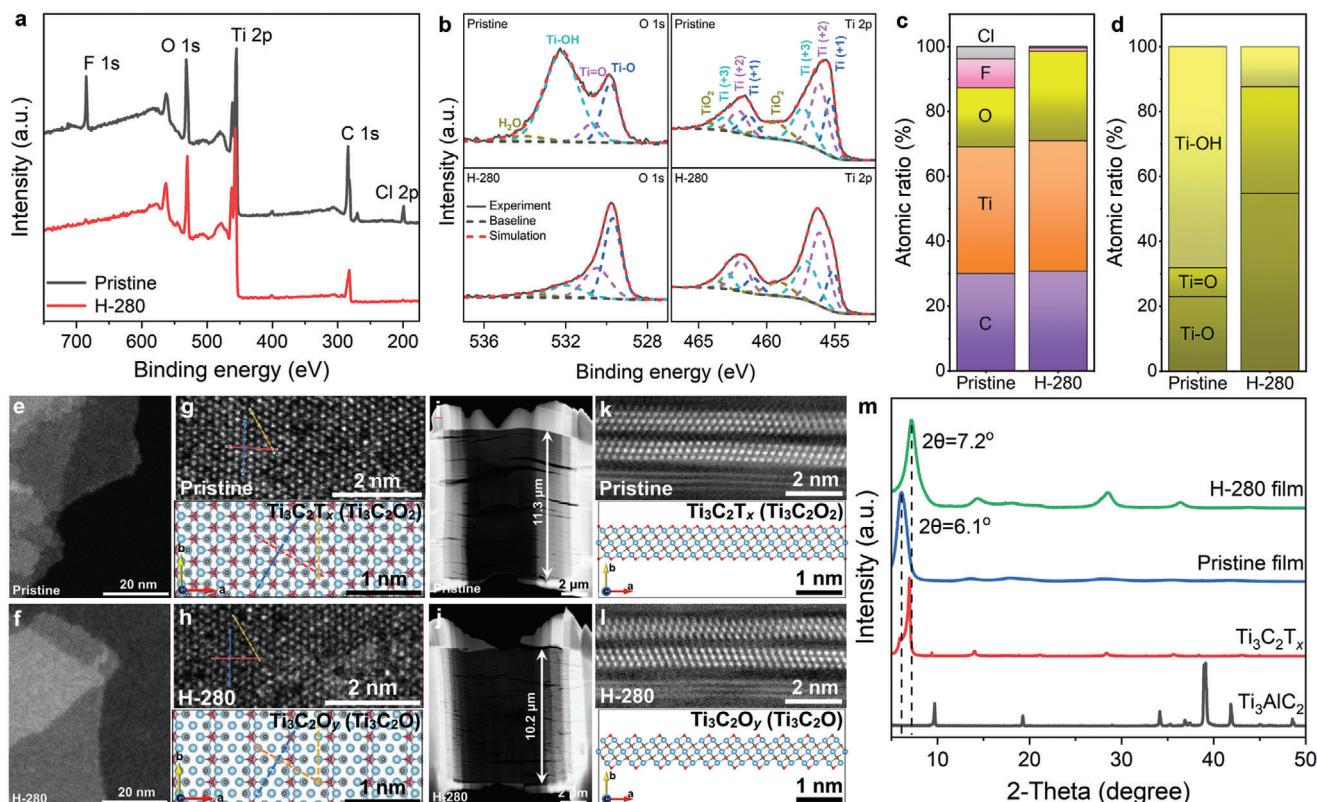**2408892 (2 of 10)**

Figure 2. Characterization of the pristine $Ti_3C_2T_x$ and sample hydrothermally treated at 280 °C for 20 h (H-280). a) XPS spectra of the pristine $Ti_3C_2T_x$ film and H-280 film. b) High-resolution O 1s and Ti 2p spectra of the pristine $Ti_3C_2T_x$ film and H-280 film. c,d) Percentage distribution of elements from EDS test (c) and oxygen-containing functional groups from XPS test (d) of the pristine $Ti_3C_2T_x$ film and H-280 film. e,f) HAADF STEM images of the delaminated pristine $Ti_3C_2T_x$ (e) and H-280 (f) flakes. g,h) HAADF STEM images of the monolayer pristine $Ti_3C_2T_x$ (g) and H-280 (h) flakes viewed along the [0001] direction. i–l) Cross-section HAADF STEM images of the pristine $Ti_3C_2T_x$ (i, k) and H-280 (j, l) vacuum-filtered films dissected by FIB. Their mass loadings are 3 mg cm^{-2}. m) XRD patterns of Ti_3AlC_2 powder, $Ti_3C_2T_x$ powder without ultrasonication, and the pristine $Ti_3C_2T_x$ and H-280 films. The bottom images of (g) and (h) are the structure models of $Ti_3C_2O_2$ and Ti_3C_2O viewed along the [0001] direction, respectively. The bottom images of (k) and (l) are the cross-section structure model of $Ti_3C_2O_2$ and Ti_3C_2O, respectively. Since $Ti_3C_2O_2$, $Ti_3C_2(OH)_2$, $Ti_3C_2F_2$, and $Ti_3C_2Cl_2$ occupy ≈85% of the pristine $Ti_3C_2T_x$ and their structures are very similar along both the [0001] and cross-section directions (Figure S9, Supporting Information), $Ti_3C_2O_2$ is used as an approximation model for the pristine $Ti_3C_2T_x$. While Ti_3C_2O is the main component of H-280, herein, Ti_3C_2O is used as an approximation model for H-280.

restructuring of $Ti_3C_2T_x$ to $Ti_3C_2O_y$ is critical for achieving the expected boost in specific capacitance. Such a process requires the preferential selection of the —O group as opposed to the —OH, —F, and —Cl functional groups. Our theoretical calculation shows that the Ti—OH bond is stronger than the Ti—F/Cl bond (Table S1, Supporting Information); therefore, —F/—Cl could be substituted by —OH under certain conditions to allow the adjacent hydroxyl groups to then dehydrate into ether groups at high temperature (Equation S1, Supporting Information). Further, the theoretical calculations show that the Ti=O bond is stronger than the Ti—OH bond; thus, some isolated Ti—OH could be oxidized into Ti=O (Equation S2, Supporting Information). Based on these inferences, we developed a strategy to modify the surface terminal groups T_x to O_y. Herein, KOH (Note S2 and Figures S2 and S3, Supporting Information), as a moderate nucleophilic reagent, is used to replace the —F/—Cl with —OH terminal groups and keep the original Ti_3C_2 substrate structure at high temperature via a hydrothermal approach (the product is referred to as H-T, T is hydrothermal temperature in °C, Figure 1c). X-ray photoelectron spectroscopy (XPS) and elemental mapping

from energy dispersive spectrometry (EDS) confirm that after hydrothermal treatment, F and Cl contents decrease sharply; Meanwhile, the O content increases dramatically, compared with the pristine $Ti_3C_2T_x$ (**Figure 2a,c**; Figure S4, Supporting Information). This effect is amplified with longer hydrothermal treatment time (Figure S5, Supporting Information). High-resolution XPS spectra of O 1s show the decrease of the —OH terminal group on the surface of H-280 while the oxygen element is mainly in the form of Ti—O—Ti and Ti=O (Figure 2b,d; Figure S6, Supporting Information).[30] The combination of EDS and XPS results indicates the H-280 surface has ≈82% oxygen-terminated Ti atoms as opposed to ≈16% in the pristine $Ti_3C_2T_x$ (Tables S2 and S3 and Note S3, Supporting Information). This evidences successful reconstruction of the surface to yield primarily $Ti_3C_2O_y$ when sufficient temperatures and treatment times are chosen (e.g., 280 °C and >10 h for H-280). This approach is also suitable for HF-etched $Ti_3C_2T_x$ MXene[31] and some thicker MXenes, for example, $Nb_4C_3T_x$ (Figure S7, Supporting Information). Actually, hydrothermal treatment of MXene has been extensively reported. Due to the existence of strong oxidants (e.g., O_2 and H_2O_2) or
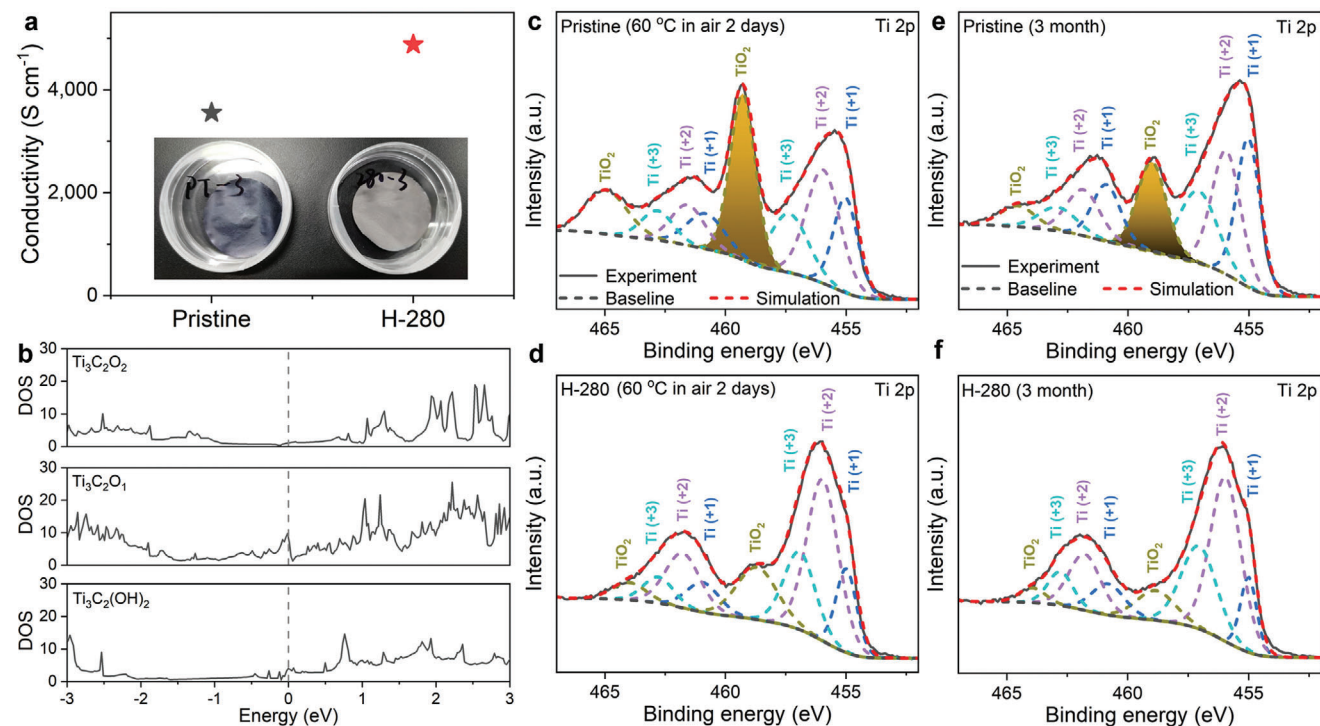
**ADVANCED
SCIENCE NEWS**

www.advancedsciencenews.com

**ADVANCED
FUNCTIONAL
MATERIALS**

www.afm-journal.de

Figure 3. Conductivity and chemical stability of the pristine $Ti_3C_2T_x$ and $Ti_3C_2O_y$ (H-280). a) Optical images and conductivities of the pristine $Ti_3C_2T_x$ film and H-280 films with mass loading of 3 mg cm^{-2}. b) Density of states (DOS) of Ti_3C_2 monolayer with different terminal groups. c,d) XPS spectra of the films that were vacuum-filtered from the pristine $Ti_3C_2T_x$ and H-280 colloidal solutions after exposure in the air at 60 °C for 2 days. For the film from the pristine $Ti_3C_2T_x$ colloidal solution, after exposing in the air at 60 °C for 2 days, a strong TiO_2 peak is detected (c). Whereas for the film from H-280, only a weak TiO_2 peak can be detected (d). e,f, XPS spectra of the films that were vacuum-filtered from the pristine $Ti_3C_2T_x$ and H-280 colloidal solutions and exposed in the air at room temperature for 3 months. After exposure in the air at room temperature for 3 months, a notable oxidation is detected in the film vacuum-filtered from the pristine $Ti_3C_2T_x$ colloidal solution (e). However, there is almost no change for the film vacuum-filtered from H-280 colloidal solution (f).

strong electrophilic reagents (e.g., H$^+$ and Li$^+$), the substrate of the MXenes would be destroyed and form large amounts of titanates or oxides during hydrothermal treatment.[23,28,29] And in the contrary, only nucleophilic substitution would happen in this work (Note S2, Supporting information).

While the hydrothermal treatment process successfully reconstructs the surface chemistry, the impact on the material structure and practical performance is equally critical. High-angle annular dark-field (HAADF) scanning transmission electron microscopy (STEM) images indicate that the bulk structure of $Ti_3C_2T_x$ has been maintained well after surface reconstruction at atomic level resolution (Figure 2e–h,k,l; Figures S8 and S9a,b, Supporting Information),[22] which has been further validated by well maintained high-resolution XPS spectra of C 1s (Figure S9c,d, Supporting Information). Moreover, the cross-section HAADF STEM images of the vacuum-filtered Ti_3C_2 films (Figure S9a,b, Supporting Information) and a shift in the (002) peak in the X-ray diffraction (XRD) pattern (Figure 2m; Figure S10, Supporting Information) confirms the decrease of interlayer spacing, which aligns with the trend in our theoretical calculations for $Ti_3C_2O_2$, $Ti_3C_2(OH)_2$, $Ti_3C_2Cl_2$, and $Ti_3C_2F_2$ (Figure S11a, Supporting Information), the successful conversion of surface terminations is further validated by a significant reduction in halogen terminal groups on the Ti_3C_2 substrate (Figure S9e,f, Supporting Information). In the case of Ti_3C_2O, the

layered structure could collapse due to the existence of numerous surface vacancies (Figure S11b, Supporting Information). However, H-280 benefits from the co-existence of Ti—O and Ti=O, which instills organization in the layered structure, suggested by a strong (002) peak in the XRD pattern (Figure 2m).

Although H-280 exhibits a transition metal oxide-like surface and TiO_2-like color, it still possesses metal-like conductivity (4880 S cm^{-1}), which is comparable to the pristine $Ti_3C_2T_x$ film (3554 S cm^{-1}, **Figure 3a**). This could be originated from the substantial electron states around the Fermi level of Ti_3C_2O and $Ti_3C_2O_2$ (Figure 3b; Figure S12, Supporting Information). Furthermore, the combination of the stable Ti_3C_2 structure and the intact oxide-like surface of H-280 (Figure 2h,l) could induce chemical and electrochemical stability, leading to long cycle life.

Chemical stability is also key for electrode materials throughout their life cycle. It is well known that MXenes are prone to oxidation in the presence of water and oxygen.[22,32–35] In the context of material and device production, an oxidation-resistant material can eliminate the expensive equipment/facilities required to provide an oxygen-free environment at scale. Excluding the influence of defects and edges,[36] we employ a work function (WF) to evaluate the oxidation stability of Ti_3C_2 with different terminal groups, where a larger WF indicates higher ability to withstand electron loss (Table S1, Supporting Information).[33,37,38] Thus, the high WFs of $Ti_3C_2O_2$ and Ti_3C_2O suggest high oxidation

**ADVANCED
SCIENCE NEWS**

www.advancedsciencenews.com

**ADVANCED
FUNCTIONAL
MATERIALS**

www.afm-journal.de
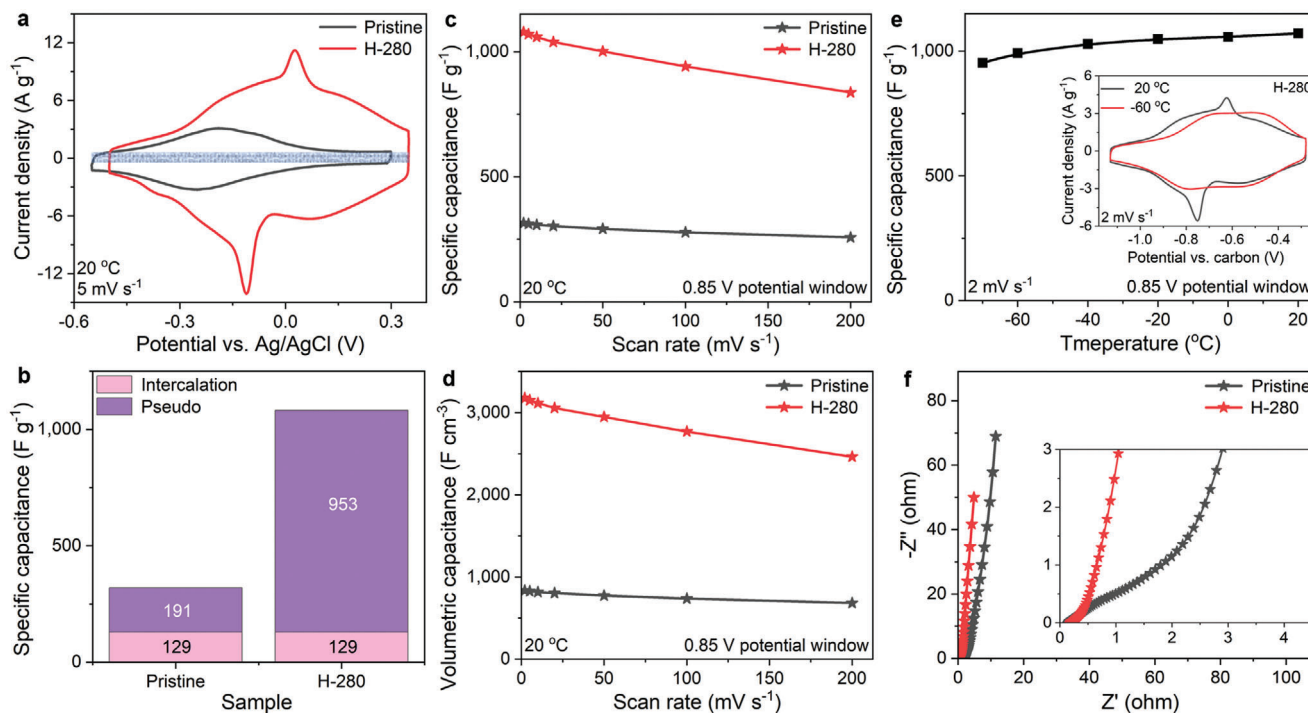
Figure 4. Electrochemical performance of the pristine $Ti_3C_2T_x$ and $Ti_3C_2O_y$ (H-280). a) Cyclic voltammograms of the pristine $Ti_3C_2T_x$ and H-280 film electrodes (mass loading of 1 mg cm^{-2}) at a scan rate of 5 mV s^{-1} with the intercalation capacitance region indicated by the shaded rectangular region. b) Specific capacitance of the pristine $Ti_3C_2T_x$ and H-280 film electrodes calculated from cyclic voltammograms at a scan rate of 5 mV s^{-1} (a). The specific capacitance from the intercalation component is approximated as 129 F g^{-1}. c,d) Gravimetric (c) and volumetric (d) rate performance of the pristine $Ti_3C_2T_x$ and H-280 film electrodes calculated from cyclic voltammograms at different scan rates. e) Specific capacitance of H-280 film electrode measured at different temperatures with a scan rate of 2 mV s^{-1}. The inset shows cyclic voltammograms of the H-280 film electrode measured at 20 and −60 °C with a scan rate of 2 mV s^{-1}. f) Electrochemical impedance spectroscopy data collected at 0.2 V for the pristine $Ti_3C_2T_x$ and H-280 film electrodes at 20 °C. The inset shows the high-frequency range. For the convenience of comparison, the intercalation capacitance of these two film electrodes was unified, which will not affect the fact that there is a sharp rise in the pseudo-capacitance of the H-280 film electrode.

resistance for H-280. This is supported by our observations of the H-280 colloidal solution and vacuum-filtered film, which were exposed to air at 60 °C for several days and room temperature for several months, respectively. Optical imaging and XPS verify significantly lower levels of oxidation of H-280 compared to $Ti_3C_2T_x$ (Figure S13, Supporting Information; Figure 3c–f). Further, differential scanning calorimetry (DSC) and thermogravimetric analysis (TGA) indicate that freeze-dried H-280 powder is stable in the air up to 450 °C, as opposed to the pristine $Ti_3C_2T_x$ powder that began oxidizing at ≈200 °C (Figure S14, Supporting Information). This confirms the high stability of $Ti_3C_2O_y$ MXene, potentially leading to a simple and cost-effective production of H-280-based devices.

2.2. Electrochemistry of the Nearly Full-Oxygen-Functionalized MXene

With respect to electrochemical performance, the expected and dramatic increase in gravimetric specific capacitance is obtained with the H-280 film electrode when compared to the pristine $Ti_3C_2T_x$ film (**Figure 4a,b**). Excluding the intercalation component of specific capacitance (also denoted as EDL; that is, the shaded rectangular part in Figure 4a, ≈129 F g^{-1}; 110 C g^{-1}), the pseudo-capacitance component increases fivefold from

191 F g^{-1} (162 C g^{-1}) in the pristine $Ti_3C_2T_x$ film electrode to 953 F g^{-1} (810 C g^{-1}) in the H-280 film electrode for a potential window of 0.85 V (Figure 4b; Figure S15, Supporting Information), which is 77% to 84% of the theoretical pseudo capacitance of Ti_3C_2O and $Ti_3C_2O_2$, respectively. This agrees very well with the expectations based on the percentage of oxygen-terminated Ti on the surface of $Ti_3C_2T_x$ (16.3%) and H-280 (82.3%). The ultrahigh specific capacitance is well validated by in situ electrochemical UV–vis spectroscopy measurements, in which electron transfer occurs in nearly all titanium atoms on the surface of Ti_3C_2. (Figure S16, Supporting Information). It is also noted that a new pair of broad redox peaks (≈0.1 V vs Ag/AgCl in 5 M H_2SO_4, Figure 4a; Figures S15 and S17, Supporting Information) appear for H-280, indicating two kinds of oxidation reactions on the surface of $Ti_3C_2O_y$. Ti—O—Ti contributes the strong peaks at −0.2 V that overlap with the redox peaks located at 0.1 V (Figure 4a).[22] Thus, the new redox peaks are attributed to Ti=O that originates from the in situ oxidation of the isolated Ti—OH at higher hydrothermal temperature (Equation S2, Supporting Information). Contrary to TiO_2 in the oxidized $Ti_3C_2T_x$,[39] Ti=O in H-280 instills excellent cycling stability even in high concentration H_2SO_4 electrolyte (5 м). More than 98% capacity has been maintained after 50000 cycles (Figure S18, Supporting Information), which far exceeds that of traditional transition metal oxide electrodes (e.g.,

**ADVANCED
SCIENCE NEWS**

www.advancedsciencenews.com

**ADVANCED
FUNCTIONAL
MATERIALS**

www.afm-journal.de

<5000 cycles).[13,40] This benefit stems from the ultra-high structural and chemical stability of the H-280 electrode (Figure S19, Supporting Information).

In addition to high specific capacitance (Figure 4c), the dense layered structure of H-280 (Figure 2j) yields high volumetric capacitance for the H-280 film electrode ($\approx$3182 F cm^{-3} or 2705 C cm^{-3} for a potential window of 0.85 V, Figure 4d; Figure S20, Supporting Information), far exceeding several typical supercapacitance materials and MXene itself (Figure 1e; Figure S21 and Table S4, Supporting Information),[10,22,41–43] even graphite and Li$_4$Ti$_5$O$_{12}$ in Li-ion battery (Figure 1e). In spite of the high storage capacitance and areal capacitance ($\approx$1.2 F cm^{-2}; 1 C g^{-1}), the H-280 electrode also exhibits excellent rate performance that far surpasses that of the pristine Ti$_3$C$_2$T$_x$ film electrode with the same mass loading (Figure S22, Supporting Information). Such superior charge transfer in the H-280 film is anomalous, considering its smaller interlayer spacing. This can be well explained by the elimination of hydrophilic hydroxyl groups that restrict hydronium ion transport among the Ti$_3$C$_2$T$_x$ layers in the pristine electrode (Figure S23, Supporting Information), which is validated by the small molar mass of the intercalated ions in the pristine Ti$_3$C$_2$T$_x$ (Figure S24 and Note S4, Supporting Information) and the decreased ion transfer resistance in H-280 (Figure 4f; Figure S25, Supporting Information). In situ XRD measurements provide insight into the structural changes during the ion charging processes (Figures S26 and S27, Supporting Information). A sudden increase in the *c*-lattice parameter is observed after the onset of Ti—O—Ti reaction, and the degree of increase is positively correlated with the amount of Ti—O—Ti. This is attributed to the significant accumulation of hydronium ions on the Ti—O—Ti surface, including both intercalation capacitance and pseudo-capacitance. Such moderate expansion and contraction in the normal direction (24%) can easily be absorbed by the gaps in the layered electrode structure of H-280 to achieve robust cycling (Figure 2j).

The remarkable performance of H-280 at room temperature is effectively sustained across an incredibly wide range of temperatures. As shown in Figure 4e, the specific capacitance of the H-280 electrode decreases only 11% when temperature decreases from 20 °C to −70 °C, which can be attributed to the rapid diffusion of the hydrated ions among the layers of H-280 (Figure S28, Supporting Information). In contrast, the Ti$_3$C$_2$T$_x$ film electrode exhibited a 64.5% loss of capacity at −70 °C and a low rate of 2 A g^{-1}, due to sluggish migration of the ions in the presence of significant hydroxyl groups (Figure S29, Supporting Information). What's more, the elimination of hydroxyl groups also enables stable high-temperature cycling of H-280 (10000 cycles at 60 °C with <2% capacity loss, Figure S30, Supporting Information).

2.3. Proton Battery Based on the Nearly Full-Oxygen-Functionalized MXene

Maximizing the performance of this MXene, particularly the specific capacitance, requires additional considerations for designing practical devices beyond supercapacitors. Typically, the electrolyte provides the source of ions for supercapacitor charging. This approach would be reasonable when the electrodes have low volumetric capacity and the device has adequate space

to accommodate electrolytes to provide ions during charge and discharge. In the case of H-280, the extremely high volumetric capacitance requires an electrolyte volume that is 7.8 times that of the electrode for the present electrolyte (5 M H$_2$SO$_4$). This would sharply decrease energy density and dilute the merits of H-280 (**Figure 5a**). Therefore, we propose and evaluate a proton battery configuration where a cathode material (chemically pre-protonated Turnbull's blue analog, H-TBA,[44] Figure S31, Supporting Information) provides a much more compact ion source. Like H-280, H-TBA exhibits excellent rate performance, low-temperature tolerance, no detectable degradation after 50000 cycles, and a comparable high first cycle efficiency (>90%, Figures S32–S34, Supporting Information). Thus, H-TBA pairs well with H-280 to form a robust, high-performance proton battery (Figure 5b).

As shown in Figure 5c, CV scans performed at rates from 5 to 100 mV s^{-1} show weak deviation in the redox peaks, indicating outstanding rate performance for the proton battery. Since protons carry the charge and surface reactions play a dominant role in both the anode and cathode (Figure S35, Supporting Information), excellent low-temperature performance has also been observed. Even at −70 °C and high power (5 A g^{-1}), $\approx$35.2 Wh kg^{-1} energy density is maintained, as compared to 47 Wh kg^{-1} at 20 °C (Figure 5d; Figure S36, Supporting Information). In contrast, an activated graphene-based supercapacitor with high voltage (3.5 V) and an organic electrolyte can only provide 25 Wh kg^{-1} at room temperature based on electrode material and electrolyte mass,[40] which is 29% less than the H-280-based proton battery at −70 °C. An additional benefit of the H-280‖H-TBA proton battery is the inherent safety advantage of the aqueous electrolyte when compared to the flammable organic electrolyte used in high-voltage supercapacitors.

Compared to a traditional pseudo-capacitor,[42] electrical double-layer capacitor,[43] and lead-acid battery,[1] the H-280-based proton battery presented here provides drastic improvements in low-temperature performance, power density, and cycle life while exhibiting energy density nearing that of lead-acid batteries and much higher safety than lithium-ion batteries (Figure 5e). These attributes render the H-280-based proton battery capable of performing in applications that demand extremely high power in ultracold environments over tens of thousands of cycles with notably higher energy density than conventional supercapacitors. Furthermore, Ti$_3$C$_2$O$_y$ also exhibits excellent performance in many fields beyond electrochemical energy storage, for example, electromagnetic interference (EMI) shielding.[45,46] The high conductivity and excellent oxidation resistance promise a long lifetime for H-280 as an EMI shield, overcoming the deficient, months-long lifetime of the pristine Ti$_3$C$_2$T$_x$ in air (Figure S37, Supporting Information).

3. Conclusion

We applied a novel and facile method to tune the contents in a traditional Ti$_3$C$_2$T$_x$ MXene, achieving the accurate alternation of halide (—F, —Cl) and hydroxide (—OH) functional groups by oxygen species (Ti—O/=O) through a nucleophilic substitution reaction. The nearly full-oxygen-functionalized MXene (Ti$_3$C$_2$O$_y$) film provides ultrahigh density of Ti—O/=O redox-active sites and consequently delivers an exceptionally high specific capacitance,

ADVANCED
SCIENCE NEWS

www.advancedsciencenews.com

ADVANCED
FUNCTIONAL
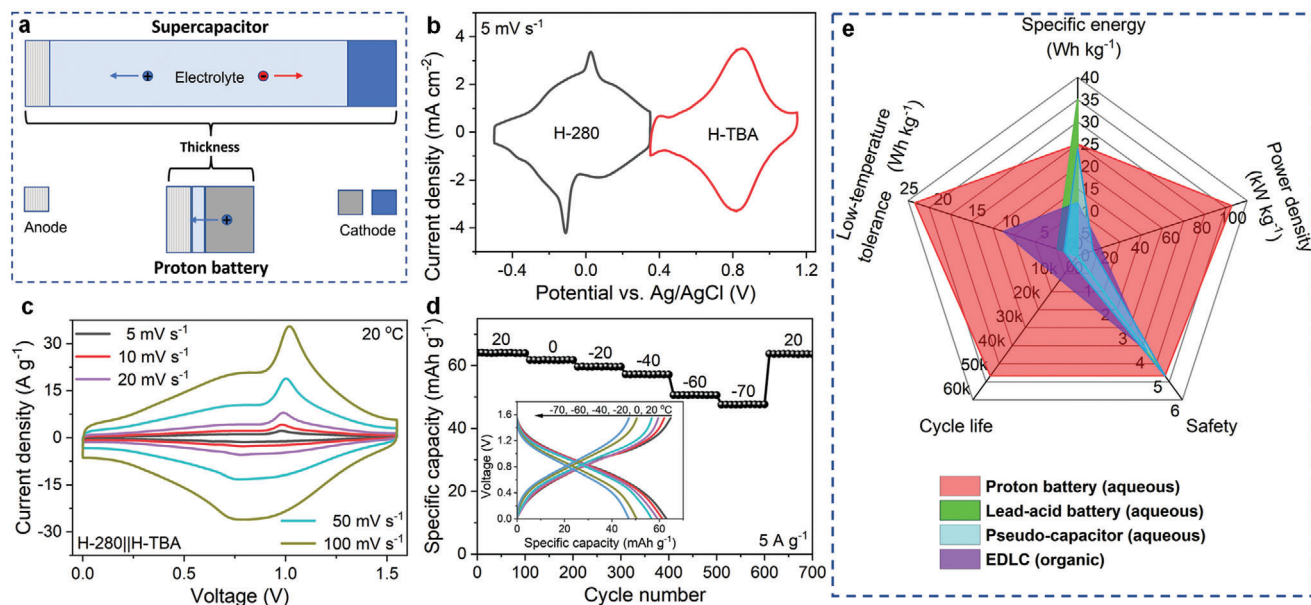**MATERIALS**

www.afm-journal.de

Figure 5. Electrochemical performance of H-280||H-TBA proton battery. a) Schematic diagrams of a supercapacitor and a proton battery using H-280 film as the anode. For the supercapacitor configuration, the volume of the electrolyte should be 5.5 times that of the H-280 film electrode. In contrast, most cations come from the counter electrode, and a small amount of electrolyte is required to wet electrodes and separator in the H-280||H-TBA hybrid battery. b) Full cell fabrication: three-electrode cyclic voltammograms of H-280 (0.3 mg cm^{-2}) and H-TBA (0.7 mg cm^{-2}) at a scan rate of 5 mV s^{-1}. c) Cyclic voltammograms of the H-280||H-TBA proton battery at different scan rates. d) Specific capacity of the H-280||H-TBA proton battery as a function of temperature during galvanostatic cycling of 5 A g^{-1}. The inset depicts galvanostatic charge–discharge profiles at different temperatures. e) Comprehensive comparison of the proton battery (device-level) in this work with a lead-acid battery, pseudo-capacitor[42] and EDLC in organic electrolyte.[43]

approximating the theoretical capacity of transition metal oxides in both aqueous and organic electrolytes. In addition, the conductive atomic level Ti—O/=O surface endows extremely fast charging/discharging in tens of seconds across a wide range of temperatures (−70 to 60 °C) in aqueous electrolyte. Together with robust structure and high chemical stability, the Ti$_3$C$_2$O$_y$ electrode achieved 98% capacity retention after 50000 cycles. When paired with pre-protonated Turnbull's blue analog, the corresponding aqueous proton batteries exhibit an energy density of 52 Wh kg^{-1} and a specific power >100 kW kg^{-1}. It can be envisioned that the structure tunability and designability of MXene will allow the further development of novel pseudocapacitive materials with even higher capacitances for high-power energy storage systems and some materials for the applications of catalysis, electromagnetic shielding, electronic and optoelectronic devices.

4. Experimental Section

Preparation of Ti$_3$C$_2$T$_x$ Colloidal Solution: A mixture of HCl and LiF was used to synthesize multilayer Ti$_3$C$_2$T$_x$ from Ti$_3$AlC$_2$ (400 mesh, 11 Technology Co., Ltd., P. R. China), similar to the method reported in the previous study.[47] In detail, 1 g of LiF was added to 20 ml of 9 M HCl solution, followed by a slow addition of 1 g of Ti$_3$AlC$_2$ with stirring in the ice bath, and then transferred to the oil bath. After etching for 36 h at 40 °C, the product was washed with deionized water by centrifuging until the pH of the supernatant reached 6. The remaining sediment (multilayer Ti$_3$C$_2$T$_x$) was mixed with 100 ml deionized water and probe sonicated (power: 400 W) for 1 h under Ar atmosphere and ice bath. Afterward, the mixture was centrifuged for 1 h at 3500 rpm. The resultant dark supernatant was a colloidal solution of a few-layer Ti$_3$C$_2$T$_x$.

Preparation of Ti$_3$C$_2$O$_y$ Colloidal Solution: The concentrated colloidal Ti$_3$C$_2$T$_x$ solution was diluted to 2 mg ml^{-1}. Next, 1.5 g KOH was slowly added into 35 ml of the diluted Ti$_3$C$_2$T$_x$ colloidal solution. The resultant suspension was transferred into 50 ml para polyphenol (PPL) lined stainless steel autoclave purged with Ar at a flow rate of 200 ml min^{-1} for 5 min (to remove the air and dissolved oxygen in the lining) and kept at 280 °C for 20 h. After cooling down to room temperature, the product was washed with 1 M H$_2$SO$_4$ (Note S2 and Figure S38, Supporting Information) and then deionized water by centrifuging until the pH of the supernatant reached ≈6. The remaining sediment was mixed with 100 ml deionized water and probe sonicated (power: 400 W) for 20 min under Ar atmosphere and ice bath to obtain Ti$_3$C$_2$O$_y$ colloidal solution (denoted as H-280). Unless stated otherwise, all hydrothermal treatment times were 20 h. For the other hydrothermal treated samples with different temperatures were denoted as H-T (T is hydrothermal temperature in °C). Due to the hydrolysis of halogen terminal groups and the subsequent dehydration of the adjacent hydroxyl terminals, the weight of the pristine Ti$_3$C$_2$T$_x$ decreases after hydrothermal treatment in KOH aqueous solution. For H-280, nearly all halogen terminal groups were substituted by hydroxyl, resulting in a mass reduction of ≈25%, yielding ≈75% after hydrothermal treatment at 280 °C in KOH aqueous solution.

Preparation of Vacuum-Filtered Ti$_3$C$_2$ Thin Film: Ti$_3$C$_2$T$_x$ or Ti$_3$C$_2$O$_y$ colloidal solution was vacuum filtered through a 25 μm thick Celgard 3501 polypropylene membrane. The wet film on the Celgard membrane was collected and dried in a vacuum overnight at 80 °C. Afterward, a flexible, free-standing Ti$_3$C$_2$T$_x$ or Ti$_3$C$_2$O$_y$ thin film was collected by peeling the thin film off the Celgard membrane. Finally, the film was pressed on a smooth Cu foil under 2 MPa.

Preparation of Chemically Pre-Protonated Turnbull's Blue Analogue (H-TBA): H-TBA was synthesized by chemical reduction of Cu^{II}[Fe^{III}(CN)$_6$]$_{2/3}$•4H$_2$O.[44] For the preparation of Cu^{II}[Fe^{III}(CN)$_6$]$_{2/3}$•4H$_2$O, typically, 50 ml of 0.2 м CuSO$_4$ solution was added dropwise into 50 ml of 0.1 м K$_3$Fe(CN)$_6$ solution under magnetic stirring. After 6 h of reaction,

**ADVANCED
SCIENCE NEWS**

www.advancedsciencenews.com

**ADVANCED
FUNCTIONAL
MATERIALS**

www.afm-journal.de

the olive-green precipitate was washed with deionized water by centrifuging 8 times and then dried in an oven at 60 °C overnight. For the chemical reduction, the as-prepared powder (0.4 g) was dispersed in 40 ml of deionized water and sonicated for 30 min. Under Ar bubbling and stirring, 20 ml of 0.05 M hydrazine solution was added dropwise to the above powder suspension. After reacting for 2 h, the crimson precipitate was washed by centrifuging 8 times and dried in a vacuum oven overnight (40 °C) to yield H-TBA powder.

Materials Characterization: X-ray diffraction (XRD) was carried out on a Bruker D8 advanced powder X-ray diffractometer equipped with copper Kα radiation (λ = 1.54 Å). The cross-sections and elementary compositions of the Ti_3C_2 thin films were characterized by a JSM-IT800 field emission scanning electron microscope (FE-SEM, JOEL) equipped with an energy-dispersive X-ray spectroscope (EDS, Oxford). Atomic-resolution characterization of the Ti_3C_2 samples was conducted on a double spherical aberration-corrected scanning transmission electron microscope (STEM, Thermo Fisher Titan Themis G2 60–300) operated at 300 kV. Single-layer Ti_3C_2 samples for high-angle annular dark-field (HAADF) STEM observation were prepared by dropping two drops of the diluted Ti_3C_2 colloidal solution onto a lacey carbon-coated copper grid (Beijing XXBR Technology Co., Ltd., P. R. China) and drying with argon flow. Foil samples of the vacuum-filtered Ti_3C_2 films for cross-section STEM observation were prepared using a Zeiss Crossbeam 540 focused ion beam (FIB). The chemical compositions of the samples were further analyzed by ESCALAB 250Xi X-ray photoelectron spectroscopy (XPS, Thermo Fisher Scientific). Peak fitting was carried out using Thermo Advantage software. The conductivities of the films were measured using an SZT-2B four probe resistivity measuring instrument (Suzhou Tongchuang Electronic Co., Ltd., P. R. China). Fourier transforms infrared (FTIR), Raman, and UV–vis spectroscopies were characterized to determine the functional groups of the vacuum-filtered Ti_3C_2 films/colloid solutions using Nicolet iS20 spectrometer, Renishaw inVia Raman microscope (633 nm He—Ne laser with a 1200 lines mm^{-1} grating, 3 mW power) and Shimadzu UV-2450 spectrophotometer, respectively. Electromagnetic interference shielding measurements were carried out in a WR-90 rectangular waveguide using a 2-port network analyzer (E5071C, Agilent Technologies, USA) in the X-band frequency range (8.2–12.4 GHz).

Electrode Preparation: In three-electrode tests, the activated carbon (AC) electrode was used as a counter electrode and prepared by mechanical processing of a pre-mixed slurry, containing 90 wt.% YP-50 AC (Kuraray, Japan), 5 wt.% Ketjen black (ECP600JD, Lion Specialty Chemicals Co., Ltd.) and 5 wt.% polytetrafluoroethylene (PTFE, 60 wt.% in water, DAIKIN, Japan) binder in ethanol. The mass loading of the obtained electrode was set as ≈15 mg cm^{-2}. For the low-temperature test, the AC electrode was pressed on platinum mesh and served as the reference electrode. In two-electrode tests, a mixture slurry of 70 wt.% H-TBA powder, 20 wt.% Ketjen carbon and 10 wt.% polyvinylidene fluoride binder (Solvay (Shanghai) Co., Ltd.) was coated on carbon fiber paper current collector to serve as a cathode.

Electrochemical Setup: All electrochemical tests in aqueous electrolytes were performed in three-electrode Swagelok cells using glass carbon as a current collector. For three-electrode tests at room temperature, Ag/AgCl in saturated KCl and Celgard 3501 membrane were used as the reference electrode and separator, respectively. For low-temperature tests, the reference electrode was changed to an AC electrode. The electrolyte was 5 M H_2SO_4 and all cells were soaked for 12 h before conducting electrochemical tests. For full cell tests, the mass ratio of the active materials in H-280 and H-TBA was set as 3:7. Electrochemical tests in organic electrolytes were performed in half coin cells. Lithium disk was used as counter and reference electrodes. 1 M LiTFSI in propylene carbonate and Celgard 2400 were used as electrolytes and separators, respectively. These coin cells were assembled in an Ar-filled glove box with O_2 and H_2O levels <0.1 ppm. All the cells were stabilized at 40 °C for 24 h before electrochemical tests.

Electrochemical Tests: Cyclic voltammetry and galvanostatic charge–discharge were performed on the CHI660E electrochemical workstation. Electrochemical impedance spectroscopy was performed using a Gamry Reference 3000 electrochemical workstation. After initially pre-cycling the

electrode 20 times at 5 mV s^{-1}, cyclic voltammetry was performed with scan rates from 2 to 200 mV s^{-1}. Galvanostatic charge–discharge (GCD) was performed at current densities from 1 to 200 A g^{-1}. Electrochemical impedance spectroscopy was performed in a frequency range from 10^{-2} to 10^5 Hz with an amplitude of 5 mV at 0.2 V. The electrochemical tests at different temperatures were performed in a high/low-temperature test chamber (GP/T-150, Guangpin Test Equipment Manufacturing Co. Ltd.). The cells were kept at the specified temperature for 2 h before electrochemical tests.

Calculations for the Electrochemical Tests: As the CV curve is non-rectangular, the specific capacity ($Q_{CV,g}$, C g^{-1}) of a single electrode, instead of the capacitance, is evaluated from the anodic scan of the CV curves based on

$$Q_{CV,g} \left(C\ g^{-1} \right) = \frac{\int i dt}{m} \tag{1}$$

here i (A) is the current changed by time t (s); m (g) is the mass of a single electrode. The volumetric capacity ($Q_{CV,v}$, C cm^{-3}) of a single electrode is calculated as the product of $Q_{CV,g}$, and the material density. For specific capacitance (C, F g^{-1}) of a single electrode, it can be calculated according to the equation $C = Q/U$, where Q represents specific capacity (C g^{-1}) and U represents potential window (V).

For the GCD curve, the specific capacity ($Q_{GCD,g}$, mAh g^{-1}) of a single electrode is evaluated using

$$Q_{GCD,g} \left(mAh\ g^{-1} \right) = \frac{I \Delta t}{3.6 m} \tag{2}$$

where I (A) is the constant current applied to the cell Δt (s) is the charge/discharging time, and m (g) is the active mass of a single electrode.

For the two-electrode cell, the specific capacity ($Q_{GCD,\ full\ cell}$, mAh g^{-1}) of the full cell was evaluated on the basis of the GCD curve:

$$Q_{GCD,full\ cell} \left(mAh\ g^{-1} \right) = \frac{I \Delta t}{3.6 m_{total}} \tag{3}$$

where m_{total} is the mass of active material on both electrodes.

The specific energy (E_{GCD}, Wh kg^{-1}) of the full cell was estimated on the basis of the discharge branch of the GCD curve:

$$E_{GCD} \left(Wh\ kg^{-1} \right) = \frac{I \left(\int_{V_0}^{V_{max}} t dV \right)}{3.6 m_{total}} \tag{4}$$

where V_0 to V_{max} is the voltage window of the full cell. Since the device in this work is a rocking-chair battery, the specific energy was estimated of the device with a coefficient of 0.5 in Figure 5e of the main text.

Electrochemical Quartz Crystal Microbalance (EQCM) Tests: For sample preparation of EQCM, the diluted $Ti_3C_2T_x$ colloidal solution was drop-coated on the surface of Au-coated quartz crystals (oscillating frequency, f_0, 5 MHz, Shenzhen RenLux Crystal Co., Ltd). After drying at room temperature overnight with nitrogen flow, the resulting ultrathin binder-free $Ti_3C_2T_x$ film had solid adhesion to the Au-coated quartz crystals and was used as the working electrode. The measurement was performed in a three-electrode system, where Ag/AgCl in saturated KCl and activated carbon were used as reference and counter electrodes, respectively. The electrolyte was 5 M H_2SO_4 and all the EQCM electrochemical measurements were performed on an electrochemical quartz crystal microbalance (eQCM 10 M, Gamry) and electrochemical workstation (Reference 3000, Gamry).

In Situ Electrochemical XRD Measurements: In situ XRD measurements were carried out on a Bruker D8 diffractometer using a modified three-electrode cell with Ti_3C_2 vacuum-filtered film, YP-50 activated-carbon film, and Ag/AgCl in saturated KCl as working, counter, and reference electrodes, respectively (Figure S39, Supporting Information). The working electrode (Ti_3C_2 film) was attached to the glass carbon using carbon nanotube film adhesive tape (JCHANO Tech Co., Ltd., P. R. China). The YP-50 film with over capacity was pressed on the platinum mesh. Further, a Kapton window was used to avoid electrolyte evaporation while allowing

X-rays to penetrate. XRD patterns were collected during cyclic voltammetry measurements at a slow scan rate of 0.1 mV s^{-1} and small potential evolution (0.04 V) to ensure sufficient XRD granularity in the range $2\theta = 4.5$–$8.5°$ with a step of $0.01°$.

In Situ Electrochemical UV–vis Spectroscopy Measurements: In situ UV–vis measurements were carried out on a Shimadzu UV-2450 spectrophotometer equipped with an integrating sphere using a modified two-electrode cell with Ti_3C_2 vacuum-filtered film and YP-50 activated-carbon film as working and counter+reference electrodes, respectively (Figure S40, Supporting Information). The working electrode (Ti_3C_2 film, 1 mg cm^{-2}) was attached to the glass, and graphite paper with a central opening was used as a current collector to be connected to the Ti_3C_2 film. The YP-50 film with high areal loading ($\approx$30 mg cm^{-2}) was attached to the graphite paper. Celgard 3501 and 5 M H_2SO_4 were used as separators and electrolytes, respectively. UV–vis spectra were collected during cyclic voltammetry measurements at a slow scan rate of 0.5 mV s^{-1} and small potential evolution ($\approx$0.027 V) to ensure sufficient UV–vis granularity in the range of 350–900 nm^{-1} with a step of 10 nm s^{-1}. Different from the previously reported method,[48] spectra signals were collected through the reflection method.

Computational Method: All density functional theory (DFT) calculations were performed with the Vienna Ab Initio Simulation Package (VASP). The exchange correlation energy was calculated by using Perdew–Burke–Ernzerhof (PBE) functional within the generalized gradient approximation (GGA). The projector augmented wave (PAW) method was employed to describe the electron-ionic cores interaction. The cutoff energy for the plane-wave basis set was 500 eV. The convergence threshold for the iteration in electronic structure calculation was set to be 10^{-6} eV, and that for geometry optimizations was set to be 0.02 eV Å^{-1}. When modeling the isolated MXene monolayers, a 15 Å spacing of vacuum was added in the Z-direction as an adjustment between computational accuracy and cost to avoid the spurious interaction between the adjacent layers. To study the c-lattice parameters of $Ti_3C_2T_2$ in water, DFT calculations were performed using 1×3×1 $Ti_3C_2T_2$ supercell. The $Ti_3C_2T_2$ supercell was formed by expansion of the unit cell, and inserted with 4 H_2O (0.67 H_2O molecules per $Ti_3C_2T_2$). The work function can be obtained from the energy difference between the vacuum level and the Fermi level.

Supporting Information

Supporting Information is available from the Wiley Online Library or from the author.

Conflict of Interest

The authors declare no conflict of interest.

Data Availability Statement

The data that support the findings of this study are available from the corresponding author upon reasonable request.

[1] E. Pomerantseva, F. Bonaccorso, X. L. Feng, Y. Cui, Y. Gogotsi, *Science* **2019**, *366*, eaan8285.
[2] H. Liu, Z. Zhu, Q. Yan, S. Yu, X. He, Y. Chen, R. Zhang, L. Ma, T. Liu, M. Li, R. Lin, Y. Chen, Y. Li, X. Xing, Y. Choi, L. Gao, H. S.-y. Cho, K. An, J. Feng, R. Kostecki, K. Amine, T. Wu, J. Lu, H. L. Xin, S. PingOng, P. Liu, *Nature* **2020**, *585*, 63.
[3] D. Wang, C. Zhou, A. S. Filatov, W. Cho, F. Lagunas, M. Wang, S. Vaikuntanathan, C. Liu, R. F. Klie, D. V. Talapin, *Science* **2023**, *379*, 1242.
[4] P. Simon, Y. Gogotsi, *Nat. Mater.* **2008**, *7*, 845.
[5] P. Simon, Y. Gogotsi, B. Dunn, *Science* **2014**, *343*, 1210.
[6] V. Augustyn, P. Simon, B. Dunn, *Energy Environ. Sci.* **2014**, *7*, 1597.
[7] L. Jiang, Y. Lu, C. Zhao, L. Liu, J. Zhang, Q. Zhang, X. Shen, J. Zhao, X. Yu, H. Li, X. Huang, L. Chen, Y.-S. Hu, *Nat. Energy* **2019**, *4*, 495.
[8] A. Ferris, S. Garbarino, D. Guay, D. Pech, *Adv. Mater.* **2015**, *27*, 6625.
[9] P. Simon, Y. Gogotsi, *Nat. Mater.* **2020**, *19*, 1151.
[10] C. Choi, D. S. Ashby, D. M. Butts, R. H. DeBlock, Q. Wei, J. Lau, B. Dunn, *Nat. Rev. Mater.* **2020**, *5*, 5.
[11] H. Sun, L. Mei, J. Liang, Z. Zhao, C. Lee, H. Fei, M. Ding, J. Lau, M. Li, C. Wang, X. Xu, G. Hao, B. Papandrea, I. Shakir, B. Dunn, Y. Huang, X. Duan, *Science* **2017**, *356*, 599.
[12] C. Zhong, Y. Deng, W. Hu, J. Qiao, L. Zhang, J. Zhang, *Chem. Soc. Rev.* **2015**, *44*, 7484.
[13] T. Zhai, L. Wan, S. Sun, Q. Chen, J. Sun, Q. Xia, H. Xia, *Adv. Mater.* **2017**, *29*, 160416.
[14] S. Fleischmann, J. B. Mitchell, R. Wang, C. Zhan, D. Jiang, V. Presser, V. Augustyn, *Chem. Rev.* **2020**, *120*, 6738.
[15] T. S. Mathis, N. Kurra, X. Wang, D. Pinto, P. Simon, Y. Gogotsi, *Adv. Energy Mater.* **2019**, *9*, 1902007.
[16] C. Choi, D. S. Ashby, D. M. Butts, R. H. DeBlock, Q. Wei, J. Lau, B. Dunn, *Nat. Rev. Mater.* **2020**, *5*, 5.
[17] H.-S. Kim, J. B. Cook, S. H. Tolbert, B. Dunn, *J. Electrochem. Soc.* **2015**, *162*, A5083.
[18] H. Tang, W. Chen, N. Li, Z. Hu, L. Xiao, Y. Xie, L. Xi, L. Ni, Y. Zhu, *Energy Storage Mater.* **2022**, *48*, 335.
[19] D. Feng, T. Lei, M. R. Lukatskaya, J. Park, Z. Huang, M. Lee, L. Shaw, S. Chen, A. A. Yakovenko, A. Kulkarni, J. Xiao, K. Fredrickson, J. B. Tok, X. Zou, Y. Cui, Z. Bao, *Nat. Energy* **2018**, *3*, 30.
[20] V. Nicolosi, M. Chhowalla, M. G. Kanatzidis, M. S. Strano, J. N. Coleman, *Science* **2013**, *340*, 1226419.
[21] M. Downes, C. E. Shuck, B. McBride, J. Busa, Y. Gogotsi, *Nat. Protoc.* **2024**, *19*, 1807.
[22] M. R. Lukatskaya, S. Kota, Z. Lin, M.-Q. Zhao, N. Shpigel, M. D. Levi, J. Halim, P.-L. Taberna, M. W. Barsoum, P. Simon, Y. Gogotsi, *Nat. Energy* **2017**, *2*, 17105.
[23] X. Zhang, X. Liu, Y. Feng, S. Qiu, Y. Shao, Q. Liao, H. Li, Y. Liu, *Appl. Mater. Today* **2022**, *27*, 101483.
[24] X. Chen, Y. Zhu, M. Zhang, J. Sui, W. Peng, Y. Li, G. Zhang, F. Zhang, X. Fan, *ACS Nano* **2019**, *13*, 9449.
[25] M. Saraf, B. Chacon, S. Ippolito, R. W. Lord, M. Anayee, R. Wang, A. Inman, C. E. Shuck, Y. Gogotsi, *Adv. Funct. Mater.* **2023**, *34*, 2306815.
[26] A. Saha, N. Shpigel, Rosy, N. L., S. Taragin, T. Sharabani, H. Aviv, I. Perelshtein, G. D. Nessim, M. Noked, Y. Gogotsi, *Adv. Funct. Mater.* **2021**, *31*, 2106294.

**ADVANCED
SCIENCE NEWS**

www.advancedsciencenews.com

**ADVANCED
FUNCTIONAL
MATERIALS**

www.afm-journal.de

[27] M. Peng, L. Wang, L. Li, X. Tang, B. Huang, T. Hu, K. Yuan, Y. Chen, *Adv. Funct. Mater.* **2022**, *32*, 2109524.

[28] S. Zheng, J. Ma, K. Fang, S. Li, J. Qin, Y. Li, J. Wang, L. Zhang, F. Zhou, F. Liu, K. Wang, Z.-S. Wu, *Adv. Energy Mater.* **2021**, *11*, 2003835.

[29] Y. Dong, Z.-S. Wu, S. Zheng, X. Wang, J. Qin, S. Wang, X. Shi, X. Bao, *ACS Nano* **2017**, *11*, 4792.

[30] W. Bao, X. Tang, X. Guo, S. Choi, C. Wang, Y. Gogotsi, G. Wang, *Joule* **2018**, *2*, 778.

[31] J. Xu, Y. Gu, B. Hu, H. Yang, D. Sha, J. Lian, S. Ge, *Chem. Commun.* **2024**, *60*, 5739.

[32] C. J. Zhang, S. Pinilla, N. McEvoy, C. P. Cullen, B. Anasori, E. Long, S.-H. Park, A. Seral-Ascaso, A. Shmeliov, D. Krishnan, C. Morant, X. Liu, G. S. Duesberg, Y. Gogotsi, V. Nicolosi, *Chem. Mater.* **2017**, *29*, 4848.

[33] K. Li, X. Wang, S. Li, P. Urbankowski, J. Li, Y. Xu, Y. Gogotsi, *Small* **2020**, *16*, 1906851.

[34] S. Huang, V. N. Mochalin, *Inorg. Chem.* **2019**, *58*, 1958.

[35] S. Huang, V. Natu, J. Tao, Y. Xia, V. N. Mochalin, M. W. Barsoum, *J. Mater. Chem. A* **2022**, *10*, 22016.

[36] T. S. Mathis, K. Maleski, A. Goad, A. Sarycheva, M. Anayee, A. C. Foucher, K. Hantanasirisakul, C. E. Shuck, E. A. Stach, Y. Gogotsi, *ACS Nano* **2021**, *15*, 6420.

[37] J. A. Yuwono, N. Birbilis, K. S. Williams, N. V. Medhekar, *J. Phys. Chem. C* **2016**, *120*, 26922.

[38] T. Schultz, N. C. Frey, K. Hantanasirisakul, S. Park, S. J. May, V. B. Shenoy, Y. Gogotsi, N. Koch, *Chem. Mater.* **2019**, *31*, 6590.

[39] Y. Xia, T. S. Mathis, M.-Q. Zhao, B. Anasori, A. Dang, Z. Zhou, H. Cho, Y. Gogotsi, S. Yang, *Nature* **2018**, *557*, 409.

[40] H. Chen, L. Hu, M. Chen, Y. Yan, L. Wu, *Adv. Funct. Mater.* **2014**, *24*, 934.

[41] W. Chen, J. Gu, Q. Liu, M. Yang, C. Zhan, X. Zang, T. A. Pham, G. Liu, W. Zhang, D. Zhang, B. Dunn, Y. M. Wang, *Nat. Nanotech.* **2022**, *17*, 153.

[42] J. C. Russell, V. A. Posey, J. Gray, R. May, D. A. Reed, H. Zhang, L. E. Marbella, M. L. Steigerwald, Y. Yang, X. Roy, C. Nuckolls, S. R. Peurifoy, *Nat. Mater.* **2021**, *20*, 1136.

[43] Y. Zhu, S. Murali, M. D. Stoller, K. J. Ganesh, W. Cai, P. J. Ferreira, A. Pirkle, R. M. Wallace, K. A. Cychosz, M. Thommes, D. Su, E. A. Stach, R. S. Ruoff, *Science* **2011**, *332*, 1537.

[44] H. Jiang, W. Shin, L. Ma, J. J. Hong, Z. Wei, Y. Liu, S. Zhang, X. Wu, Y. Xu, Q. Guo, M. A. Subramanian, W. F. Stickle, T. Wu, J. Lu, X. Ji, *Adv. Energy Mater.* **2020**, *10*, 2000968.

[45] J. Zhang, Y. Zhao, X. Guo, C. Chen, C.-L. Dong, R.-S. Liu, C.-P. Han, Y. Li, Y. Gogotsi, G. Wang, *Nat. Catal.* **2018**, *1*, 985.

[46] C. Wang, S. Chen, L. Song, *Adv. Funct. Mater.* **2020**, *30*, 2000869.

[47] J. Xu, X. Hu, X. Wang, X. Wang, Y. Ju, S. Ge, X. Lu, J. Ding, N. Yuan, Y. Gogotsi, *Energy Storage Mater.* **2020**, *33*, 382.

[48] D. Zhang, R. Wang, X. Wang, Y. Gogotsi, *Nat. Energy* **2023**, *8*, 567.

2408892 (10 of 10)